



# Additive noise models for photoacoustic spatial coherence theory

BROOKE STEPHANIAN,<sup>1</sup> MICHELLE T. GRAHAM,<sup>2</sup> HUAYU HOU,<sup>2</sup> AND MUYINATU A. LEDIJU BELL<sup>1,2,\*</sup>

<sup>1</sup>Department of Biomedical Engineering, Johns Hopkins University, Baltimore, MD, USA

<sup>2</sup>Department of Electrical and Computer Engineering, Johns Hopkins University, Baltimore, MD, USA

\*[mledijubell@jhu.edu](mailto:mledijubell@jhu.edu)

**Abstract:** Directly displaying the spatial coherence of photoacoustic signals (i.e., coherence-based photoacoustic imaging) remarkably improves image contrast, signal-to-noise ratio (SNR), contrast-to-noise ratio (CNR), and imaging depth when compared to conventional amplitude-based reconstruction techniques (e.g., backprojection, delay-and-sum beamforming, and Fourier-based reconstruction). We recently developed photoacoustic-specific theory to describe the spatial coherence process as a function of the element spacing on a receive acoustic aperture to enable photoacoustic image optimization without requiring experiments. However, this theory lacked noise models, which contributed to significant departures in coherence measurements when compared to experimental data, particularly at higher values of element separation. In this paper, we develop and implement two models based on experimental observations of noise in photoacoustic spatial coherence measurements to improve our existing spatial coherence theory. These models were derived to describe the effects of incident fluence variations, low-energy light sources (e.g., pulsed laser diodes and light-emitting diodes), averaging multiple signals from low-energy light sources, and imaging with light sources that are > 5mm from photoacoustic targets. Results qualitatively match experimental coherence functions and provide similar contrast, SNR, and CNR to experimental SLSC images. In particular, the added noise affects image quality metrics by introducing large variations in target contrast and significantly reducing target CNR and SNR when compared to minimal-noise cases. These results provide insight into additional requirements for optimization of coherence-based photoacoustic image quality.

© 2018 Optical Society of America under the terms of the [OSA Open Access Publishing Agreement](#)

## 1. Introduction

Photoacoustic imaging requires light transmission and optical absorption of a target, which undergoes local heating and thermal expansion and generates a sound wave [1, 2]. This sound wave is subsequently detected with conventional ultrasound receivers. Spatial coherence is a measurement of the similarity of the recorded pressure distribution across the aperture of the acoustic receivers, and this measurement can be leveraged to overcome one of the primary limitations of photoacoustic imaging — i.e., limited optical penetration. This limitation exists because photoacoustic signals are not generated in the absence of optical absorption. Similarly, in the presence of low optical absorption at depth, shallower regions that experience greater absorption, tend to dominate photoacoustic images created with image reconstruction techniques that display differences in signal amplitudes. These limitations are particularly evident with recent advances in smaller and portable low-energy light sources, such as pulsed laser diodes [3–7] or light emitting diodes [8–10].

Photoacoustic image reconstruction techniques that utilize the spatial coherence of recorded pressure distributions include coherence factor (CF) weighting to mitigate sidelobe-associated clutter [11]. The combination of CF weighting and the minimum variance beamforming has also been shown to enhance both spatial resolution and contrast [12]. Similarly, CF and synthetic aperture focusing have been used together to improve lateral resolution and signal-to-noise

ratios (SNRs) [13]. A SNR-dependent CF was additionally introduced for adaptive side lobe suppression in photoacoustic imaging [14].

Short-lag spatial coherence (SLSC) imaging shares many of the same benefits of the coherence-based imaging techniques described above, but it differs by directly displaying spatial coherence information rather than using coherence as a weighting metric for amplitude-based images. SLSC imaging was initially developed for ultrasound imaging [15] and later applied to photoacoustic imaging of targets ranging from brachytherapy seeds in phantoms, *ex vivo* tissue, and *in vivo* canine prostates [16–18] to blood vessel phantoms consisting of either India ink solution [19, 20] or flexible rubber rods [5, 21, 22]. This technique was also applied to image graphite rods and larger spherical inclusions created from a graphite-titanium-gelatin mixture, both surrounded by gelatin [23]. These applications of SLSC imaging consistently demonstrated improvements in contrast in high-noise imaging environments, particularly in the presence of low laser fluence and when targets were located at large distances from the light source. SLSC is primarily useful in imaging tasks aimed at identifying the presence or absence of a photoacoustic signal (e.g., interventional imaging to identify tool tips or brachytherapy seeds). Similar to the CF weighing methods described above, SLSC images have also been weighted with conventional delay-and-sum (DAS) photoacoustic images to reduce acoustic clutter and improve DAS image quality [24], thus providing additional promise for amplitude-dependent tasks, such as spectral unmixing.

While initial experimental results with SLSC imaging have shown outstanding promise when compared to both DAS and Fourier-based reconstruction methods [25], the theoretical basis for coherence-based photoacoustic imaging is still being explored [19, 20], and current models do not simulate various noise conditions that are observed in experimental data. The absence of noise models in coherence-based photoacoustic theory limits accurate modeling of the observed benefits of averaging coherence data measured from multiple acquisitions (particularly when using low-energy laser sources [5]). In addition, the lack of noise models is expected to be responsible for many of the deviations observed between noiseless theoretical spatial coherence functions and experimental data [19, 20].

The purpose of this paper is to explore noise models that mimic observations from previously acquired experimental data. In particular, spatial coherence functions from brachytherapy seeds of length 4.5 mm and 0.8 mm outer diameter exhibit a familiar linear decrease in the short-lag region, but the surrounding noise regions have a degree of randomness in the coherence measurements that is not modeled with existing theory [16]. Similarly, photoacoustic data acquired with pulsed laser diodes have low coherence at lag one and this coherence rises with averaging [5]. These two trends are not described with existing photoacoustic spatial coherence theory [19, 20]. Therefore, this paper introduces, develops, and tests the limits of two noise models that mimic these two experimental observations that are not included in noiseless models of theoretical spatial coherence. These noise models are then evaluated in the context of SLSC imaging.

## 2. Theory

### 2.1. Background

Our current theory states that the normalized spatial coherence,  $C(u)$ , of a lateral cross section of a photoacoustic target at the imaging depth,  $z$ , is equal to a scaled Fourier transform of the square of the product of the initial acoustic pressure distribution,  $A$ , and the distribution of optical absorbers,  $\chi$ , in the lateral dimension of the imaging plane,  $x$ , as defined by the equation:

$$C(u) \propto e^{-j2\pi x_k u} \cdot \int_{-\infty}^{\infty} z^{-2} |\chi A|^2 e^{-j2\pi x u} dx \quad (1)$$

where  $x_k$  corresponds to the lateral positions of interest in the image (i.e., the locations of lateral lines after beamforming). The initial pressure distribution  $A$  depends on the size- and shape-dependent product of the optical fluence distribution,  $F$ , and two tissue-related parameters: the Grüneisen parameter,  $\Gamma$ , and optical absorption,  $\mu_a$ , such that

$$A = \Gamma \mu_a F. \quad (2)$$

Note that  $\chi$  and  $A$  are both functions of  $x$  and  $z$ , and Eq. (1) considers their cross sectional profiles at a specific depth  $z$  and multiple  $x$  positions. The spatial frequency  $u$  depends on  $z$ , the spatial lag,  $m$ , which is reported in units of element number, the array pitch (i.e., the constant spacing between elements), and the acoustic wavelength,  $\lambda$ , as defined by the equation:

$$u = \frac{m \times \text{pitch}}{\lambda z}. \quad (3)$$

One pixel in a photoacoustic SLSC image is then created by integrating the spatial coherence function up to a specific short-lag value,  $M$ , over the multiple frequencies within the -6 dB bandwidth of the ultrasound probe:

$$SLSC_{pixel}(x_k, z) = \frac{1}{\lambda_H - \lambda_L} \int_{\lambda_L}^{\lambda_H} \int_0^M C(u) dm d\lambda \approx \frac{1}{N_\lambda} \sum_{\lambda=\lambda_L}^{\lambda_H} \sum_{m=1}^M C(u) \quad (4)$$

where  $\lambda_H$  and  $\lambda_L$  correspond to the highest and lowest acoustic frequencies within the -6dB array bandwidth, respectively, and  $N_\lambda$  is the number of wavelengths used in numerical simulations that implement Eq. (4).

## 2.2. Noise models derived from empirical observations

The following descriptions of our noise models are based on two observations of spatial coherence functions obtained from experimental data (i.e., they are phenomenological models), whereas Section 2.3 provides a mathematical foundation for our observations. The first observation is that there is randomness in the coherence estimates that appears to be independent of the lag value. The second observation is that the coherence at lag 1 for pulsed laser diodes is significantly lower than the lag-zero value, and this lag-one coherence increases with temporal averaging. These two

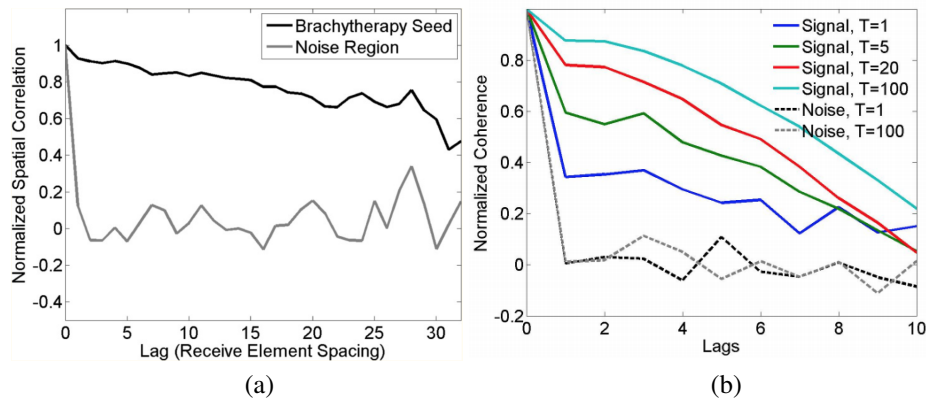


Fig. 1. Examples of experimental data showing (a) random noise in coherence functions [16] and (b) increased lag-one coherence when averaging signals received from a pulsed laser diode, where  $T$  represents the number of frames that were averaged before calculating the coherence functions [5]. These figures were reproduced with permission from Refs. [5, 16].

observations are illustrated in Fig. 1, and we hypothesize that they originate from two sources of noise that can be modeled independently.

We model the random noise in experimental coherence functions,  $\mathcal{N}$ , by adding random values drawn from a standard, zero-mean, normal distribution to the theoretical coherence functions described by Eq. (1). The standard deviation of the distribution is  $\sigma_N$ , which indicates that 99.7% (i.e., approximately 100%) of the noise values are within the range:

$$\mathcal{N} \in [-3\sigma_N, 3\sigma_N] \quad (5)$$

The additional noise observed with low-energy lasers is modeled as a delta function that is scaled by a noise-to-signal ratio ( $NSR$ ) defined as:

$$NSR = \frac{C(u)|_{m=1}}{C(0)} \quad (6)$$

where  $C(0)$  and  $C(u)|_{m=1}$  are the values of spatial coherence function evaluated at lags  $m = 0$  and  $m = 1$ , respectively. We then assume that this noise model acts as an additional contribution to the coherence function that would exist without this noise (i.e., when  $NSR = 0$ ). Therefore, we can combine the two noise models (i.e., random Gaussian noise,  $\mathcal{N}$ , and  $NSR \cdot \delta[m]$ ) and normalize by the maximum value of this combination to arrive at a new expression that describes a normalized theoretical photoacoustic spatial coherence in the presence of the two noise sources that we observe in our experimental data. For fixed values of  $\lambda$  and  $z$ , this expression reduces to a function of  $m$ :

$$C_{noise}(m) = \frac{1}{K} \left[ C(m) + \mathcal{N} + \frac{C(1)}{C(0)} \delta[m] \right] \quad (7)$$

where  $K$  is introduced to normalize the spatial coherence function to a value of 1 at lag  $m = 0$ . This normalization factor,  $K$ , is considered to be the constant of proportionality needed to remove the proportional relationship noted in Eq. (1), which would otherwise exist in Eq. (7) as well.

### 2.3. Mathematical foundations to support noise models

Although Eq. (7) was derived based on empirical observations, it can also be derived by first noting that random variations in the fluence distribution incident on a target (e.g., caused by scattering or random photon travel) contribute to noise in the coherence estimates. These random variations have a direct impact on the initial pressure distribution,  $A$ , of Eq. (1). Therefore, we can describe the pressure distribution containing source-related noise,  $A'$ , as the sum of a noiseless term,  $A$ , and an uncorrelated noise term,  $N_A$ , which we model as drawn from a normal distribution, such that:

$$A' = A + N_A \quad (8)$$

Substituting Eq. (8) into Eq. (1) and noting that  $\chi$  is a random variable that describes the absorber distribution in the absence of noise, we achieve the following expression to model the spatial coherence of signals that contain source-related noise contributions,  $C'(u)$ :

$$C'(u) \propto \frac{e^{-j2\pi x_k u}}{z^2} \cdot \int_{-\infty}^{\infty} |\chi A + N_A|^2 e^{-j2\pi x u} dx \quad (9)$$

Eq. (9) reduces to the sum of two Fourier transforms, each multiplied by a phase term:

$$C'(u) \propto \frac{e^{-j2\pi x_k u}}{z^2} \cdot \left[ \int_{-\infty}^{\infty} |\chi A|^2 e^{-j2\pi x u} dx + \int_{-\infty}^{\infty} |2\chi A N_A + N_A^2| e^{-j2\pi x u} dx \right] \quad (10)$$

The product of the phase term and the first Fourier transform is proportional to Eq. (1). We define the product of the phase term and the second Fourier transform as proportional to  $\mathcal{N}$ , which simplifies to:

$$C'(u) \propto C(u) + \mathcal{N} \quad (11)$$

Next, we note that normalized spatial coherence in the presence of source-related noise can also be defined in terms of the normalized correlations between two signals  $S_i$  at location  $i$  on an array and  $S_{i+m}$  at a location separated by  $m$  elements from location  $i$ :

$$C'(u) = \frac{\int S_i S_{i+m}}{\sqrt{\int S_i^2 \int S_{i+m}^2}} \quad (12)$$

where the integration is performed over the time dimension of the recorded signals (which is related to the depth dimension through the speed of sound). Assume that the signals measured by the channels of this array are corrupted by additional independent uncorrelated noise  $N_i$  and  $N_{i+m}$ , which represent system-related noise associated with the receiver electronics (rather than noise associated with the photoacoustic source). We can then define a correlation,  $C_{noise}$ , as:

$$C_{noise} = \frac{\int (S_i + N_i)(S_{i+m} + N_{i+m})}{\sqrt{\int (S_i + N_i)^2 \int (S_{i+m} + N_{i+m})^2}} \quad (13)$$

According to Eq. (13),  $C_{noise}$  is equal to 1 when  $m = 0$ . After assuming that the system-related noise and received signals are uncorrelated when  $m \neq 0$ , Eq. (13) can be simplified to:

$$C_{noise} = \frac{\int S_i S_{i+m}}{\sqrt{\int (S_i^2 + N_i^2) \int (S_{i+m}^2 + N_{i+m}^2)}} \quad (14)$$

We then assume that the signal power,  $P_S$ , on any two elements of the array is the same and the noise power is given by  $P_N$ . Eq. (12) can then be rewritten as a function of  $P_S$ , and Eq. (14) can be rewritten as functions of  $P_S$ ,  $P_N$ , and  $C'(u)$ :

$$\begin{aligned} C_{noise} &= \frac{P_S \cdot C'(u)}{P_S + P_N} \\ &= \frac{1}{1 + P_N/P_S} \cdot C'(u) \end{aligned} \quad (15)$$

Based on the combination of Eq. (13) and Eq. (15) and the definition of  $u$  provided in Eq. (3), as  $P_N$  increases,  $C_{noise}$  remains as 1 when  $u = 0$ , and  $C_{noise}$  is a lower-amplitude version of  $C'(u)$  when  $u \neq 0$ , such that [26]:

$$C_{noise}(u) = \begin{cases} 1, & u = 0 \\ \frac{1}{1 + P_N/P_S} \cdot C'(u), & u \neq 0 \end{cases} \quad (16)$$

which supports rearrangement of Eq. (16) as the sum of  $C'(u)$  plus a delta function scaled by the noise-to-signal power ratio, when  $0 \leq u < D/\lambda z$ , where  $D$  is the total width of the array:

$$C_{noise}(u) = \frac{1}{K_0} \left[ \frac{P_N}{P_S} \delta[u] + C'(u) \right] \quad (17)$$

$K_0$  is introduced to normalize Eq. (17) to a value of 1 when  $u = 0$ .

After substituting Eq. (11) into Eq. (17), the resulting expression can be simplified to:

$$C_{noise}(u) = \frac{1}{K} \left[ C(u) + \mathcal{N} + \frac{P_N}{P_S} \delta[u] \right] \quad (18)$$

where  $K$  represents the normalization term in the presence of the two noise sources.

We use the mathematical description provided by Eq. (18) to relate physical terms to the noise models described in Section 2.2. Specifically,  $\mathcal{N}$  describes the fluence variations (which occur due to scattering and random photon travel, regardless of the laser energy), and  $\frac{C(u)|_{m=1}}{C(0)}$  is equal to the ratio between the additive noise power on each channel and the signal power (i.e., the noise-to-signal power ratio,  $\frac{P_N}{P_S}$ ). This ratio is related to the receiver electronics sensitivity, which dictates the  $NSR$  that can be achieved with a particular photoacoustic system configuration (including a photoacoustic system that uses low-energy energy light sources). Fig. 1(b) demonstrates that temporal averaging of signals from a low-energy laser decreases this  $NSR$ .

### 3. Methods

#### 3.1. Simulation methods

Theoretical SLSC images were created from a simulated 2D phantom with a circular target of high optical absorption surrounded by a low optical absorption background, using the theory described in Section 2. The magnitude of the initial pressure distribution inside and outside of the target, across the lateral dimension of the imaging plane, (i.e.,  $A$ ), was equal to  $5.93 \mu\text{J}/\text{cm}^3$  and  $0.13 \text{ nJ}/\text{cm}^3$ , respectively. Specifically, the distribution was obtained based on the following parameters: an average fluence  $F = 130 \text{ mJ}/\text{cm}^2$  incident on the lateral dimension of the imaging plane, the Grüneisen parameter,  $\Gamma$ , set to 0.144 and 0.81 inside and outside of the target, respectively, and the optical absorption,  $\mu_a$ , set to  $111 \text{ cm}^{-1}$  and  $0.1 \text{ cm}^{-1}$  inside and outside of the target, respectively. The expected value of the optical absorber distribution,  $\chi$ , was modeled as a constant value of 1. The target diameter was varied from 2 mm to 20 mm in increments of 2 mm, unless otherwise noted.

The simulated ultrasound array had 128 elements, 0.3 mm pitch, and frequencies of 3 MHz to 7.25 MHz in 0.25 MHz increments. The short-lag values,  $M$ , ranged from  $M = 5$  to 20 (which corresponded to 3.9% to 15.6% of the 128-element aperture). The values of  $\sigma_N$  were 0, 0.1, 0.2, 0.5, and 1.0, and the  $NSR$  values were 0, 0.25, 0.50, 0.75, 1.0, and 1.5, unless otherwise stated.

#### 3.2. In vivo liver data

We acquired data from a hepatic blood vessel in an *in vivo* porcine liver and created spatial coherence functions and SLSC images of the blood vessel using previously described methods based on Eq. (12) [16]. Our photoacoustic imaging system included an Alpinion E-Cube 12R ultrasound scanner connected to an Alpinion L3-8 linear array transducer (Alpinion, Seoul, Korea), which was synchronized with a Phocus Mobile Nd:YAG-based laser (Optoek Inc., Carlsbad, CA) operating at 750 nm. A 5 mm diameter fiber bundle coupled to the laser output transmitted an incident energy of 40 mJ per pulse to the tissue surface. A laparotomy was performed to gain access to the liver, and the ultrasound probe and fiber bundle were both in direct contact with the liver tissue. This study was approved by the Johns Hopkins Animal Care and Use Committee.

#### 3.3. Performance metrics

The relationships among signal-to-noise ratio (SNR), contrast-to-noise ratio (CNR), and contrast measurements in theoretical SLSC images were quantified as functions of short-lag value,  $M$ , and target diameter,  $d$ . To calculate these image quality metrics for theoretical and *in vivo* images, two regions of interest (ROIs) were identified inside and outside the target at the same axial depth.

Rectangular ROIs were selected to include the maximum signal amplitude, and a second ROI of the same size at the same depth was located laterally to the right of the target. The ROIs were 1.6 mm (axial)  $\times$  2.7 mm (lateral), and the distance between the right edge of the target ROI and left edge of its matching lateral ROI was 1.5 cm. The SNR, CNR, and contrast were defined as:

$$SNR = \frac{\mu_{in}}{\sigma_{out}} \quad (19)$$

$$CNR = \frac{|\mu_{in} - \mu_{out}|}{\sqrt{\sigma_{in}^2 + \sigma_{out}^2}} \quad (20)$$

$$Contrast = 20 \log_{10} \left( \frac{\mu_{in}}{\mu_{out}} \right) \quad (21)$$

where  $\mu_{in}$  and  $\mu_{out}$  are the mean of signal amplitudes within ROIs inside and outside of the target, respectively, and  $\sigma_{in}$  and  $\sigma_{out}$  is the standard deviations of the signal amplitudes within ROIs inside and outside of the target, respectively.

Spatial coherence functions, SLSC image cross-sectional profiles, contrast, CNR, and SNR measurements obtained with our theory were compared to experimental results published in six previous papers [5, 16–18, 22, 23] and to the *in vivo* data described in Section 3.2 in order to assist with theory validation and to offer explanations for previous trends across a wide range of data types (i.e., phantoms, *ex vivo* tissue, and *in vivo*). It would therefore be helpful to view the results presented in this paper alongside the experimental results presented in Refs. [5, 16–18, 22, 23].

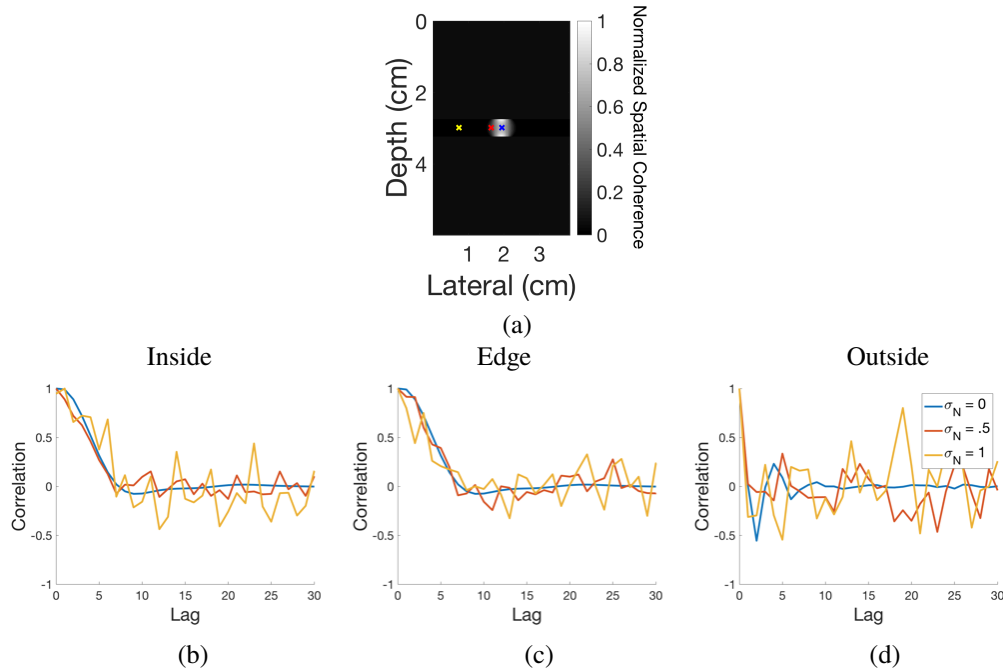


Fig. 2. (a) Theoretical SLSC image with markers at the outside (yellow), on the edge (red), and inside (blue) of a 5 mm diameter target. Corresponding coherence functions at the marker locations are shown for the (a) inside, (b) edge, and (c) outside locations when  $\sigma_N$  is 0, 0.5, and 1.0 for the a 5 mm diameter target.

## 4. Results

### 4.1. Simulation results

Fig. 2(a) shows the SLSC image of a circular target with a 5 mm diameter. The coherence functions corresponding to selected points of interest inside, on the edge, and outside of the target are shown in Fig. 2(b)-(d), with the locations of the points of interest marked in the SLSC image. For each of these locations,  $\mathcal{N}$  was varied to assess the modeled effects of fluence-related noise on the spatial coherence functions. The fluence-related noise model that closely resembled the noise observed in previous experiments had  $\sigma_N$  values ranging from 0.5 to 1.

For visual comparison of the effect of  $\sigma_N$  on simulated SLSC images, Fig. 3 shows SLSC images created with various  $\sigma_N$  values. Qualitatively, the images generally demonstrate increased randomness of the coherence inside and outside of each target as  $\sigma_N$  increases for each short-lag value,  $M$ . The increased randomness is expected to reduce image SNR and CNR and introduce more randomness in corresponding contrast measurements. In addition, contrast appears to be reduced as  $M$  increases from 5 to 20. The axial line plots shown in Fig. 3 were taken from a lateral line corresponding to the target center in the associated SLSC images. Results from three  $M$  values were combined into one plot for each noise level. These axial line plots are later used to evaluate both qualitative and quantitative relationships among contrast and  $M$ .

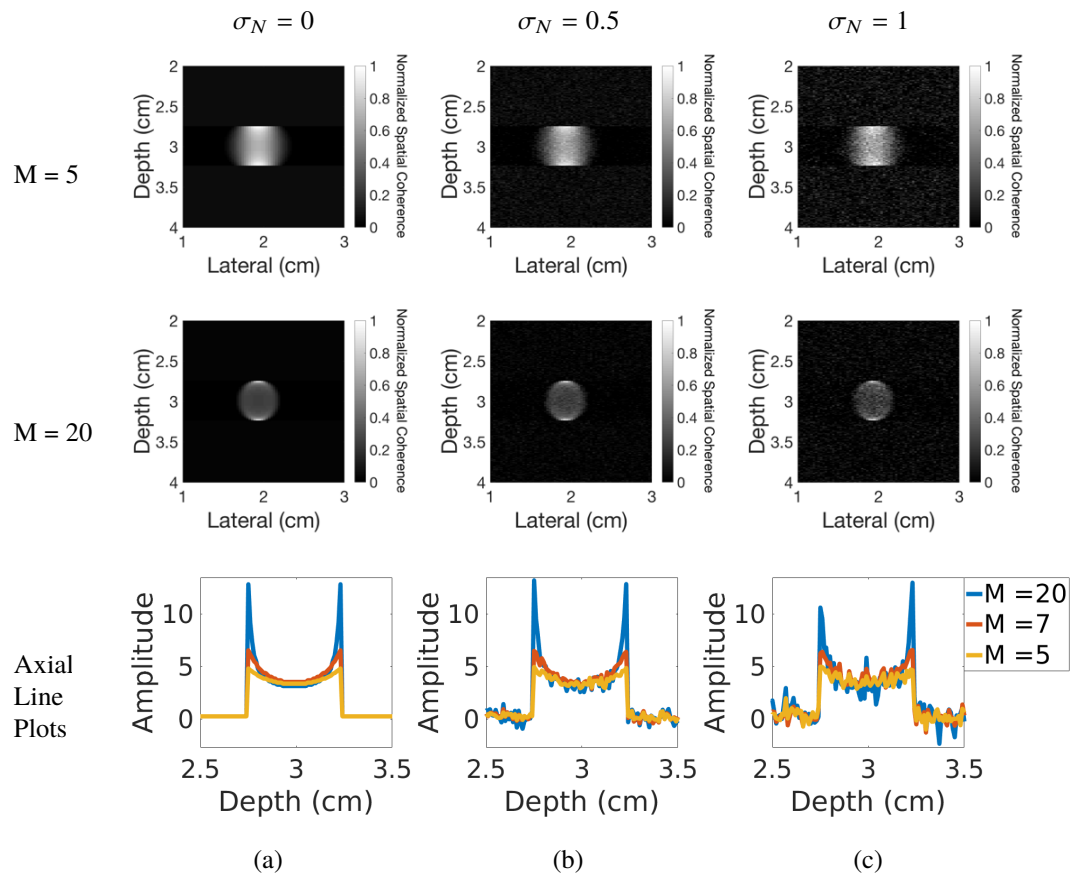


Fig. 3. SLSC images of a 5 mm diameter target when  $\sigma_N$  is (a) 0, (b) 0.5, and (c) 1.0, displayed with short-lag values of  $M = 5$  and 20 and the corresponding axial line plots taken at the lateral position corresponding to the target center.

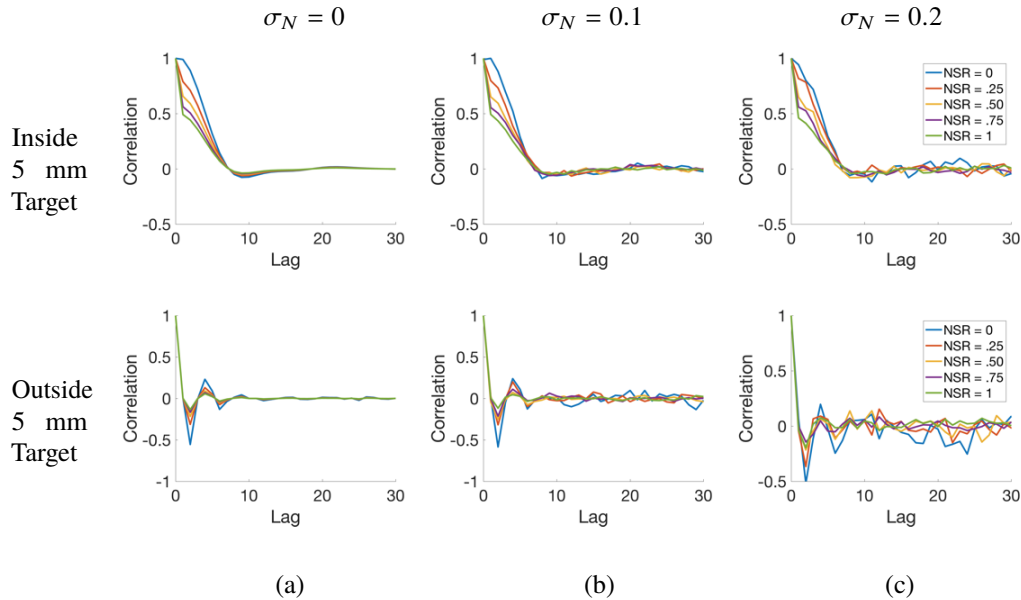


Fig. 4. Spatial coherence functions inside and outside a 5 mm diameter target shown with  $NSR$  values of 0, 0.25, 0.5, 0.75, and 1 and  $\sigma_N$  values of (a) 0, (b) 0.1, and (c) 0.2.

Fig. 4 shows the effect of including the noise model that simulates the lower coherence observed with low-energy laser sources. The first column contains no variations in fluence (i.e.,  $\sigma_N = 0$ ). In this first column, as  $NSR$  increases from 0 to 1, the coherence functions inside the target start to exhibit the low coherence that is observed in experimental data acquired with pulsed laser diodes rather than Nd:YAG lasers. The coherence functions obtained with the Nd:YAG laser is more representative of the results obtained with  $NSR = 0$  (see Fig. 1(a)). Previous work has also shown that averaging signals from multiple laser firings enables us to recover similar spatial coherence to that measured with Nd:YAG lasers (see Fig. 1(b)), and the results in Fig. 4 show that this effect of averaging can be modeled by decreasing the  $NSR$  value.

When outside of the target, decreasing the  $NSR$  value increases the absolute value of the coherence that is measured when  $\text{lag} \geq 1$ , relative to that measured with  $NSR = 0$ , which is not observed experimentally [5]. However, the addition of fluence-related noise,  $\sigma_N$ , in the second and third columns of Fig. 4 better represents our experimental observations, particularly when  $NSR > 0$ . In these cases, the increasing  $NSR$  has minimal impact on the variations observed in the coherence functions obtained outside of the target. This behavior is consistent with previously observed experimental measurements (e.g., Fig. 1(b)), indicating that both  $NSR$  and  $\sigma_N$  in Eq. (7) must be greater than zero to adequately model the noise observed in experimental data. Thus, the fluence-related noise (i.e.,  $\sigma_N$ ) adds randomness to the coherence measured at all lags and this randomness increases as the value of  $\sigma_N$  increases and affects both the coherence measured within and outside of the photoacoustic target.

For visual comparison of the effect of both  $\sigma_N$  and  $NSR$  on simulated SLSC images, Fig. 5 shows SLSC images created with Eq. (18) replacing the  $C(u)$  term in Eq. (4) for various  $\sigma_N$  and  $NSR$  values and a short-lag value of  $M = 5$ . Qualitatively, as  $NSR$  increases, the images in Fig. 5 do not appear to be affected, which is likely due to  $NSR$  only adjusting lag 1 relative to lag 0 and the coherence functions are always normalized to 1 at lag 0. However, similar to Fig. 3, as  $\sigma_N$  increases, the randomness of coherence inside and outside of the target increases, for both values of  $NSR$ . These results indicate that the fluence-related noise (i.e.  $\sigma_N$ ) decreases SLSC image

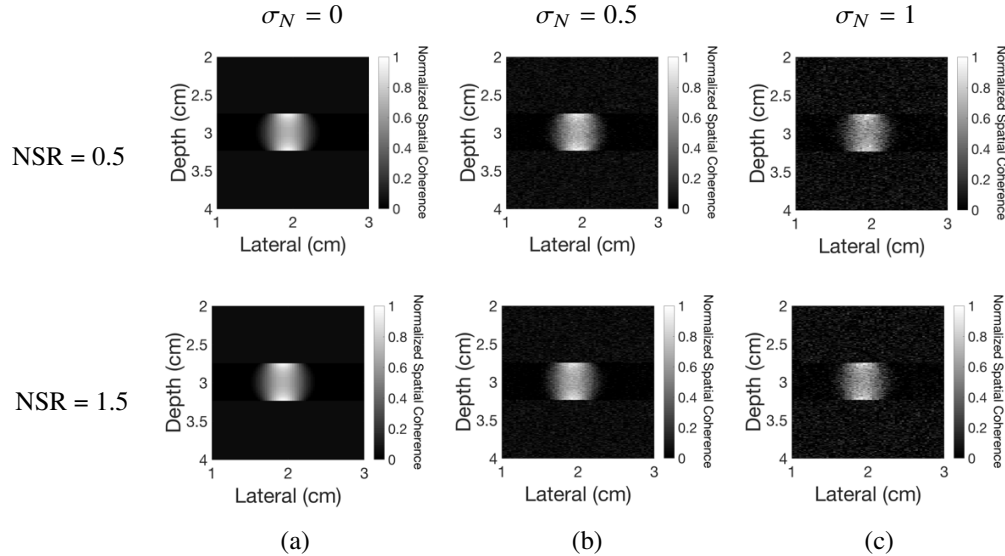


Fig. 5. SLSC images for NSR values of 0.5 and 1.5 and  $\sigma_N$  values of (a) 0, (b) 0.5, and (c) 1.0 for a 5 mm diameter target and  $M = 5$ .

SNR and CNR, while noise due to a combination of system receiver electronics, low-energy laser sources, and minimal or no averaging (i.e., noise represented by  $NSR$ ) have minimal impact on SLSC image contrast, which is generally consistent with experimental observations (e.g., Fig. 3 in Ref. [5]). However, this trend was not observed in Table 1 of Ref. [23], which shows increasing contrast with averaging. The difference between these trends likely occurs because of differences in the implementation of averaging. Signals were averaged prior to computing normalized cross correlations to form SLSC images in Ref. [5], while SLSC images were averaged in Ref. [23].

Fig. 6 shows changes in the theoretical SLSC images as target size increases in the absence of a noise model. Qualitatively, contrast decreases as target size increases, which can also be appreciated by axial line plots through the central lateral position of each target in the SLSC images. Fig. 7(a) shows these axial line plots for the same target sizes shown in Fig. 6 but with added noise (i.e.,  $\sigma_N = 0.1$  and  $NSR = 0.5$ ). Fig. 7(b) shows similar line plots with a higher magnitude of added noise (i.e.,  $\sigma_N = 1.3$  and  $NSR = 0.5$ ). In both noise cases, as target size increases, a decrease in contrast is observed. In addition, the coherence signal difference between the target boundaries and target center increases as target size increases. Qualitatively, the line plots for the higher noise levels seem to match line plots obtained in both experimental and *in vivo* data [18, 22], particularly in the background of the image (i.e., outside of the target). This

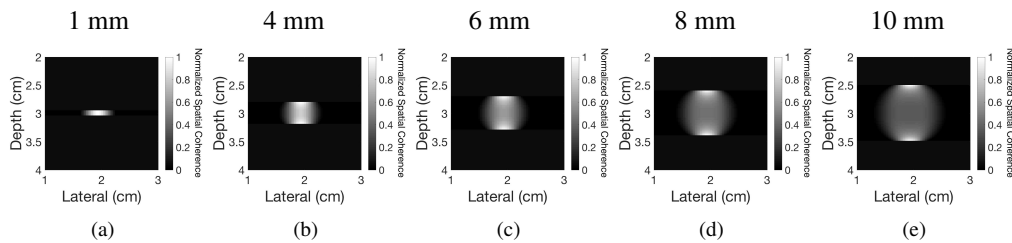


Fig. 6. SLSC Images with target diameters of (a) 1, (b) 4, (c) 6, (d) 8, and (e) 10 mm, created with  $M = 5$  and no noise in the model.

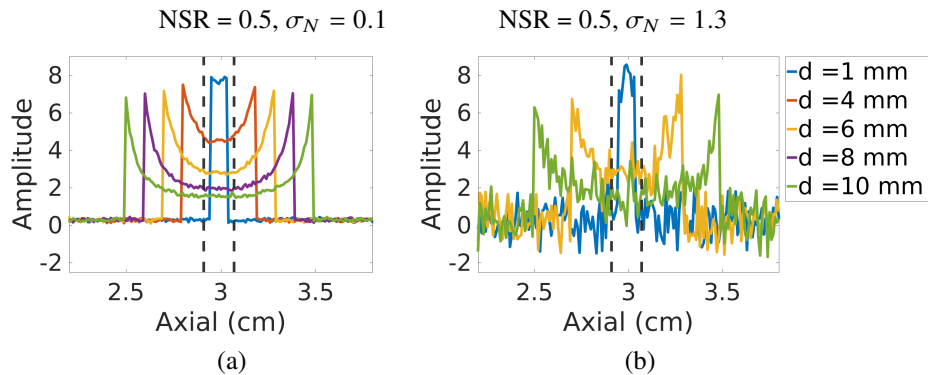


Fig. 7. Axial line plots taken at the lateral location corresponding to the target center for 1 mm, 4 mm, 6 mm, 8 mm, and 10 mm diameter circular targets with noise values of (a)  $\sigma_N = 0.1$  and  $\text{NSR} = 0.5$  and (b)  $\sigma_N = 1.3$  and  $\text{NSR} = 0.5$  and  $M = 5$ . Target sizes of 4 mm and 8 mm were omitted from the line plots in Fig. 7(b) to assist with plot readability. The vertical lines show axial boundaries of the ROIs used to measure contrast, CNR, and SNR.

similarity can be confirmed by comparing Fig. 7(b) with Fig. 9(b) in [22] and Fig. 5 in [18].

Contrast as a function of target size in the presence of the noise model described by Eq. (7) is shown for both low ( $\sigma_N = 0.1$ ) and high ( $\sigma_N = 1.3$ ) values of  $N$  in Figs. 8(a) and 8(b), respectively. Confirming our qualitative observations, the best contrast with the theoretical data is observed at smaller targets, as well as at higher lag values (e.g.,  $M = 10$ ) for the smaller targets. Contrast decreases as target size increases from 2 mm to 20 mm, and there is minimal contrast difference when varying the short-lag values (i.e.,  $M$ ) of the larger targets. Contrast values are as high as 24.66 dB with lower noise and the maximum contrast increases to 27 dB with increased noise. The contrast measurement is also more variable as the fluence-related noise (i.e.,  $\sigma_N$ ) increases, which indicates that this noise is responsible for the large standard deviations observed in previous measurements of contrast (e.g. Fig. 6 in Ref. [16]).

For larger target sizes, the similar contrast measured across multiple short-lag values seems to contradict our observations in Fig. 3, where the contrast appears to decrease as the short-lag value increases from  $M = 2$  to  $M = 20$  for a 5 mm-diameter target. However, the corresponding axial line plots in Fig. 3 demonstrate an increase in the coherence of the target boundaries with increasing  $M$ , while the target center coherence remains relatively constant as  $M$  increases, which explains this apparent discrepancy. The SLSC images in Fig. 3 were normalized to the brightest pixel in each image (which occurs at the target boundaries), and this normalization causes a perceived qualitative contrast decrease when comparing SLSC images created with increasing short-lag values. However, because the ROI for calculating contrast (indicated by the vertical lines in Fig. 7) is located at the target center and excludes the target boundaries, the calculated contrast remains relatively constant across the different  $M$  values.

CNR as a function of target size is shown for both low ( $\sigma_N = 0.1$ ) and high ( $\sigma_N = 1.3$ ) values of  $N$  in Figs. 8(c) and 8(d), respectively. Unlike the contrast measurements in Fig. 8(b), there is a significant decrease in CNR when higher values of  $\sigma_N$  are included in the theoretical predictions. CNR values are as high as 33.18 with lower noise and the maximum CNR decreases to 4.5 with the addition of more noise. The CNR plots in Fig. 8(c) each experience a peak for target diameters ranging from 6-8 mm for lower  $\sigma_N$  values, but the measured CNR generally decreases as target size increases beyond 4 mm for the higher  $\sigma_N$  values, as shown in Fig. 8(d). The peaks in CNR measurements occur because of the location and size of the chosen ROI. Fig. 7 shows that for targets smaller than 6 mm in diameter, the ROI includes an increase in coherence caused by the narrower target width near the circular boundary, which results in a larger standard

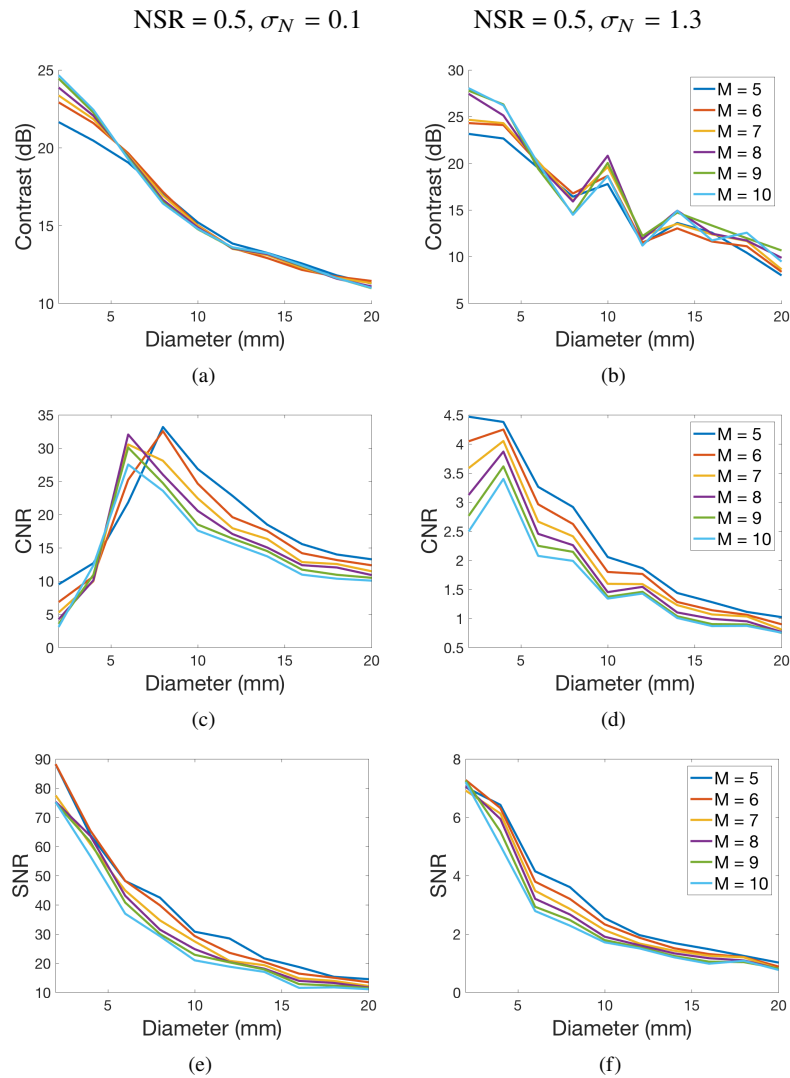


Fig. 8. (a,b) Contrast, (c,d) CNR, and (e,f) SNR as a function of diameter with  $NSR = 0.5$  and  $\sigma_N$  values (a,c,e) 0.1 and (b,d,f) 1.3.

deviation within the target region and a lower CNR.

SNR as a function of target size is shown for both low ( $\sigma_N = 0.1$ ) and high ( $\sigma_N = 1.3$ ) values of  $N$  in Figs. 8(e) and 8(f), respectively. Similar to the CNR measurements, there is an order of magnitude decrease in the measured SNR when the higher  $\sigma_N$  value is included in the theoretical predictions. SNR values are as high as 88.23 with lower noise values and the maximum value decreases to 7.0 with the increased noise. SNR also decreases as target diameter increases.

As shown in the axial line plots of Fig. 7, although the mean signal coherence remains relatively constant as noise increases, the standard deviation of signals within the target and background ROIs significantly increase as the noise level increases. Therefore, the trends of decreasing CNR and SNR with increasing noise levels are caused by the increased standard deviations of signals within the target and background regions of the SLSC images.

To demonstrate examples of required noise values to achieve similar performance to that observed in previous experimental data, Table 1 shows previously measured contrast, CNR, and

Table 1. Previously reported contrast, CNR, and SNR measurements from experimental SLSC images and corresponding  $\sigma_N$  and  $NSR$  values required to achieve these measurements. Lag is reported as a percentage of the receive aperture

	Bell, <i>et al.</i> 2013 [16]	Bell, <i>et al.</i> 2014a [18]	Bell, <i>et al.</i> 2014b [5]	Pourebahimi, <i>et al.</i> 2013 [23]
Target	brachytherapy seed (in phantom)	brachytherapy seed ( <i>in vivo</i> )	vessel phantom	graphite inclusion
Target Width	4.5 mm*	4.5 mm*	4 mm	4 mm
Laser	Nd:YAG	Nd:YAG	pulsed diode	Nd:YAG
Laser Energy	11.2 mJ	6.3 - 10.5 mJ	2.4 - 8 $\mu$ J	-
Laser Fluence	178 mJ/cm <sup>2</sup>	100 - 167 mJ/cm <sup>2</sup>	-	30 mJ/cm <sup>2</sup>
Lag	6%	12%	12%	28%
Contrast (dB)	23 - 28	5 - 25	14 - 27	33.8 - 44.9
SNR	2.5 - 4.5	1 - 4	3 - 35	14.3 - 39
CNR	2.5 - 5	2 - 5	N/A	14 - 38.7
$\sigma_N$	0.8	0.9	0.2 - 1.3	0 - 0.3
$NSR$	0.5	0.2	0 - 8.5	4 (contrast only) 0.2 (CNR & SNR)

\*These targets (i.e., brachytherapy seeds) appear as rectangular cross sections and were compared to circular targets of the same diameter as the lateral width of the rectangle.

SNR values reported in published papers [5, 16, 18, 23] and lists the parameters that are needed for our model to match these values. In particular, we matched the reported lateral target size to a circular disk of the same size and adjusted the  $NSR$  and  $\sigma_N$  values in our model until the resulting measurements matched the reported measurements. We also matched the short-lag value as a percentage of the receive array aperture rather than matching the number of elements. The corresponding laser energies are additionally listed for comparison. The  $\sigma_N$  values ranged from 0 - 1.3 and  $NSR$  values ranged from 0 - 8.5. The ROIs used to measure contrast, CNR, and SNR with our model were placed in the same locations described in Section 2, although the ROIs were not the same as previously reported ROIs. Nonetheless, we are more interested in the noise values required for our model to achieve similar contrast, SNR, and CNR to previous reports rather than using the noise models to recreate images that match the previously reported images. Note that it was difficult to match contrast with our model applied to the parameters in Ref. [23], likely because SLSC images were averaged to achieve higher contrast, and therefore a separate  $NSR$  value is reported to match contrast only. For this value of  $NSR$  (i.e., 4), the corresponding  $\sigma_N$  was 0.2.

#### 4.2. Comparison of theory with *in vivo* liver data

Fig. 9(a) shows the ultrasound B-mode image of an *in vivo* blood vessel in the liver. Fig. 9(b) shows the corresponding photoacoustic SLSC image of the vessel created with  $M = 1$ . A theoretical SLSC image of a circular target with a diameter that matches the lateral width of the *in vivo* vessel in the B-mode image (i.e., 11.97 mm) was simulated. Although the axial dimensions of the theoretical and experimental images do not correspond (because we approximate the absorber function as circular), the results in the lateral dimension are assumed to be separable.

Representative coherence functions inside and outside of the vessel are shown in Figs. 9(c) and 9(d), respectively. When comparing the *in vivo* coherence functions to the theoretical coherence functions created without noise, the random variations at higher lags are not well modeled and there is a negative spike at the lower lags outside of the vessel. These observations support the introduction of noise models to obtain spatial coherence functions that are consistent with experimental data. We added source-related random noise,  $\mathcal{N}$ , with  $\sigma_N = 1.1$  and system-related noise with  $NSR = 1.0$  to achieve a closer match between the *in vivo* and theoretical spatial

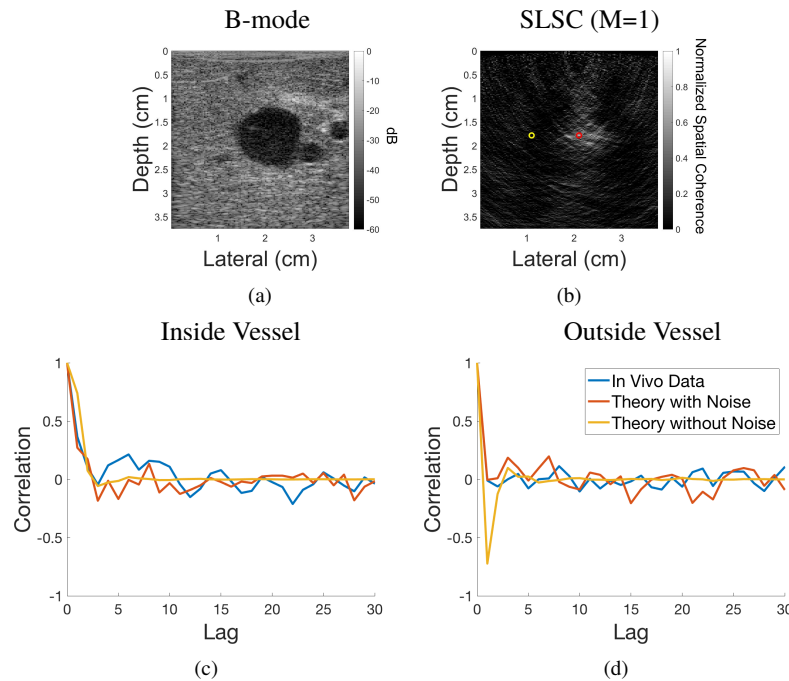


Fig. 9. (a) B-mode and (b) SLSC images from *in vivo* liver experiment. Representative coherence functions are displayed from the locations shown (c) inside and (d) outside of the target. The corresponding theoretical coherence functions were created from a target with a diameter of 11.97 mm, with noise values  $\sigma_N = 1.1$ , and  $NSR = 1.0$  where indicated.

coherence functions obtained inside and outside of the vessel. At a short-lag value of  $M = 1$ , the contrast, SNR, and CNR of the *in vivo* SLSC image were 14.0 dB, 3.6, and 1.5, respectively. The corresponding contrast, SNR, and CNR for the theoretical SLSC image were 11.3, 3.7, and 3.0, which represents 2.7 dB, 0.1, and 1.5 differences in contrast, SNR, and CNR, respectively.

## 5. Discussion

We introduced and implemented two additive noise models to simulate source-related noise (e.g., fluctuations in the initial pressure distribution) and system related noise (e.g., thermal and electronic) in spatial coherence measurements of photoacoustic data. The random additive noise model closely mimics the randomness in coherence estimates that we observe in experimental data (e.g., Figs. 1(a), 9(c), and 9(d)), which was not present in our noiseless models of photoacoustic spatial coherence [19, 20]. The mathematical descriptions in Section 2.3 relate this random noise to variations in the incident fluence distribution, which is random and known to be highly dependent on the scattering medium. Table 1 indicates that the contribution from fluence variations is generally consistent for multiple scattering environments, with  $\sigma_N$  values that span 0 - 1.3. Similarly, modeling the system-related noise as a delta function with an amplitude that is based on the ratio between the lag 1 and lag 0 spatial coherence measurements provides a working theory to explain the trends seen by Bell *et al.* [5], where averaging signals acquired with a pulsed laser diode increased the measured coherence at lag 1. The results in Table 1 and Fig. 9 are consistent with this theory because the contribution from this type of noise has a greater impact when the laser energy is lower, with  $NSR$  values that span 0.2 - 1 for Nd:YAG lasers (no averaging included [16, 18]) and 0 - 8.5 for the pulsed laser diode [5]. In comparison to the 0.2 - 1  $NSR$  values needed when no averaging is involved for the Nd:YAG laser, the  $NSR$  values can

be as high as 4 when averaging SLSC images produced with an Nd:YAG laser [23].

The inclusion of noise in the spatial coherence model lays the groundwork for estimation and predictions of expected photoacoustic SLSC image quality in experimental data and enables us to quantify expectations for a range of target sizes and short-lag values (i.e.,  $M$ ). For example, Fig. 8 shows that the smaller target lateral cross sections in the image plane can be displayed with larger  $M$  values in the presence of noise to achieve better contrast, which was also observed in previous experimental data, where the circular axis of brachytherapy seeds was displayed with higher  $M$  values than the long axis of the same seeds [16, 17]. This trend is also seen in Fig. 9, where the spatial coherence functions of the larger 1 cm target indicate that high-contrast SLSC images are limited to the lower short-lag values (e.g.,  $M = 1$ ). Another interesting observation is that the contrast measurements are more variable as  $\sigma_N$  increases, which provides a working theory to explain the large variations in contrast measurements that are typically seen in experimental data. These results indicate that these large fluctuations are caused by variations in the fluence distribution, which varies due to scattering and is also highly variable when the light source is sufficiently far from the photoacoustic target (e.g.,  $> 5$  mm, as indicated by Fig. 6 in Ref. [17]).

When these noise models are included before measuring target contrast, CNR, and SNR, these measurements more closely represent the results observed in previous experimental data [5, 16–18]. Specifically, SNR and CNR values significantly decrease with the addition of higher levels of fluence-related noise (i.e.,  $\mathcal{N}$ ), as shown in Fig. 8. In these higher noise environments, variations in the contrast measurement also increase. In comparison, the high  $NSRs$  that can be addressed with signal averaging prior to calculating spatial coherence do not appear to affect the overall image contrast, because SLSC is a correlation-based technique that is not directly dependent on signal magnitudes. Although there is minimal impact on SLSC image quality, the coherence functions are still affected by the chosen  $NSR$  value. Based on these observations, it is evident that our new noise models enable us to identify the best trade-off among contrast, CNR, SNR, and  $M$  in photoacoustic SLSC images, and this choice is based on target size.

One difference between experimental and simulated data that is not included in the noise models presented in this paper is the presence of significantly large (and often negative) values in coherence estimates, particularly at higher lag values. This could be due to a lower number of measurements of spatial coherence at the larger lags. In general, our noise models do not address the larger positive or negative values at higher lags, and this will be the focus of future work. Our future work will additionally simulate 2D absorber functions that mimic experimental data.

## 6. Conclusion

We developed and tested two models to describe the observed noise in photoacoustic spatial coherence measurements. The development of these noise models enables more realistic simulation of trends observed in experimental photoacoustic SLSC image data. These trends include random variations in the spatial coherence functions at higher lag values and changes in the contrast, CNR, and SNR image quality metrics as functions of target size and the short-lag value  $M$  that is used to display images. We have additionally provided a working theory to explain the large variations in contrast measurements that are typically seen in experimental data and the effects of averaging signals acquired with a pulsed laser diode to increase the measured coherence at lag 1. These noise models are promising for future optimization of coherence-based photoacoustic image quality.

## Funding

NSF CAREER Award (ECCS 1751522 ); NIH (R00 EB018994).

## Acknowledgments

The authors thank Kelley Kempinski and Dr. Jin He for assistance with *in vivo* data collection, and Nicholas Louloudis, Sue Eller, and Ivan George for animal care and surgery support.

## Disclosures

The authors declare that there are no conflicts of interest related to this article

## References

1. P. Beard, "Biomedical photoacoustic imaging," *Interface Focus* **1**(4), 602–631 (2011).
2. M. Xu and L. V. Wang, "Photoacoustic imaging in biomedicine," *Rev. Sci. Instrum.* **77**(4), 041101 (2006).
3. R. G. Kolkman, W. Steenbergen, and T. G. van Leeuwen, "In vivo photoacoustic imaging of blood vessels with a pulsed laser diode," *Lasers Med. Sci.* **21**(3), 134–139 (2006).
4. T. J. Allen and P. C. Beard, "Pulsed near-infrared laser diode excitation system for biomedical photoacoustic imaging," *Opt. Lett.* **31**, 3462–3464 (2006).
5. M. A. L. Bell, X. Guo, H. J. Kang, and E. Boctor, "Improved contrast in laser-diode-based photoacoustic images with short-lag spatial coherence beamforming," in *Proceedings of IEEE International Ultrasonics Symposium*, (IEEE, 2014), pp. 37–40.
6. K. Daoudi, P. Van Den Berg, O. Rabot, A. Kohl, S. Tisserand, P. Brands, and W. Steenbergen, "Handheld probe integrating laser diode and ultrasound transducer array for ultrasound/photoacoustic dual modality imaging," *Opt. Express* **22**(21), 26365–26374 (2014).
7. P. K. Upputuri and M. Pramanik, "Performance characterization of low-cost, high-speed, portable pulsed laser diode photoacoustic tomography (PLD-PAT) system," *Biomed. Opt. Express* **6**(10), 4118–4129 (2015).
8. W. Xia, M. K. A. Singh, E. Maneas, N. Sato, Y. Shigeta, T. Agano, S. Ourselin, S. J. West, and A. E. Desjardins, "Handheld real-time LED-based photoacoustic and ultrasound imaging system for accurate visualization of clinical metal needles and superficial vasculature to guide minimally invasive procedures," *Sensors* **18**(5) (2018).
9. E. Maneas, W. Xia, M. K. A. Singh, N. Sato, T. Agano, S. Ourselin, S. J. West, A. L. David, T. Vercauteren, and A. E. Desjardins, "Human placental vasculature imaging using an LED-based photoacoustic/ultrasound imaging system," in *Proc. SPIE, Photons Plus Ultrasound: Imaging and Sensing*, vol. 10494 (2018), p. 104940Y.
10. A. Hariri, J. Lemaster, J. Wang, A. S. Jeevarathinam, D. L. Chao, and J. V. Jokerst, "The characterization of an economic and portable LED-based photoacoustic imaging system to facilitate molecular imaging," *Photoacoustics* **9**, 10–20 (2018).
11. R. J. Zemp, R. Bitton, K. K. Shung, M.-L. Li, G. Stoica, and L. V. Wang, "Photoacoustic imaging of the microvasculature with a high-frequency ultrasound array transducer," *J. Biomed. Opt.* **12**(1), 010501 (2007).
12. S. Park, A. B. Karpouk, S. R. Aglyamov, and S. Y. Emelianov, "Adaptive beamforming for photoacoustic imaging," *Opt. Lett.* **33**(12), 1291–1293 (2008).
13. C.-K. Liao, M.-L. Li, and P.-C. Li, "Photoacoustic imaging with synthetic aperture focusing and coherence weighting," *Opt. Lett.* **29**(21), 2506–2508 (2004).
14. Y.-H. Wang and P.-C. Li, "SNR-dependent coherence-based adaptive imaging for high-frame-rate ultrasonic and photoacoustic imaging," *IEEE Trans on Ultrason., Ferroelectr., Freq. Control.* **61**(8), 1419–1432 (2014).
15. M. A. Lediju, G. E. Trahey, B. C. Byram, and J. J. Dahl, "Short-lag spatial coherence of backscattered echoes: imaging characteristics," *IEEE Trans on Ultrason., Ferroelectr., Freq. Control.* **58**(7) (2011).
16. M. A. L. Bell, N. Kuo, D. Y. Song, and E. M. Boctor, "Short-lag spatial coherence beamforming of photoacoustic images for enhanced visualization of prostate brachytherapy seeds," *Biomed. Opt. Express* **4**(10), 1964–1977 (2013).
17. M. A. L. Bell, X. Guo, D. Y. Song, and E. M. Boctor, "Transurethral light delivery for prostate photoacoustic imaging," *J. Biomed. Opt.* **20**(3), 036002 (2015).
18. M. A. L. Bell, N. P. Kuo, D. Y. Song, J. U. Kang, and E. M. Boctor, "In vivo visualization of prostate brachytherapy seeds with photoacoustic imaging," *J. Biomed. Opt.* **19**(12), 126011 (2014).
19. M. T. Graham and M. A. L. Bell, "Theoretical application of short-lag spatial coherence to photoacoustic imaging," in *Proceedings of IEEE International Ultrasonics Symposium*, (IEEE, 2017), pp. 1–4.
20. M. T. Graham and M. A. L. Bell, "Development and validation of a short-lag spatial coherence theory for photoacoustic imaging," in *Proc. SPIE, Photons Plus Ultrasound: Imaging and Sensing*, vol. 10494 (2018), p. 104945K.
21. M. A. L. Bell, A. K. Ostrowski, K. Li, P. Kazanzides, and E. M. Boctor, "Localization of transcranial targets for photoacoustic-guided endonasal surgeries," *Photoacoustics* **3**(2), 78–87 (2015).
22. N. Gandhi, M. Allard, S. Kim, P. Kazanzides, and M. A. L. Bell, "Photoacoustic-based approach to surgical guidance performed with and without a da Vinci robot," *J. Biomed. Opt.* **22**(12), 121606 (2017).
23. B. Pourebrahimi, S. Yoon, D. Dopsa, and M. C. Kolios, "Improving the quality of photoacoustic images using the short-lag spatial coherence imaging technique," in *Proc. SPIE, Photons Plus Ultrasound: Imaging and Sensing*, vol. 8581 (2013), p. 85813Y.
24. E. J. Alles, M. Jaeger, and J. C. Bamber, "Photoacoustic clutter reduction using short-lag spatial coherence weighted imaging," in *Proceedings of IEEE International Ultrasonics Symposium*, (IEEE, 2014), pp. 41–44.

25. M. A. L. Bell, D. Y. Song, and E. M. Boctor, "Coherence-based photoacoustic imaging of brachytherapy seeds implanted in a canine prostate," in *Proc. SPIE, Medical Imaging: Ultrasonic Imaging and Tomography*, vol. 9040 (2014), p. 90400Q.
26. N. B. Bottenus and G. E. Trahey, "Equivalence of time and aperture domain additive noise in ultrasound coherence," *The J. Acoust. Soc. Am.* **137**(1), 132–138 (2015).